crystals

MDPI

Article

Tuning CO_2 Adsorption in Metal–Organic Frameworks via Metal-Ion and Ligand Modulation

Sharon Liang [1] and Xing Kang [2,*]

[1] YK Pao School, Shanghai 201620, China; sharonlxr@hotmail.com
[2] Key Laboratory for Ultrafine Materials of Ministry of Education, School of Materials Science and Engineering, East China University of Science and Technology, Shanghai 200237, China
* Correspondence: kangxing@ecust.edu.cn

Abstract

With the aim of elucidating structure–property relationships for CO_2 capture, five MOFs with different metal nodes and linker functionalities were synthesized and evaluated. MOF-5 and MOF-5-NH_2 were constructed from Zn_4O clusters, UiO-66 and UiO-66-NH_2 from $Zr_6O_4(OH)_4$ clusters, and HKUST-1 from Cu_2 paddlewheel units. PXRD, UV–vis, SEM, and TGA confirmed phase purity, coordination, morphology, and thermal stability. CO_2 adsorption measurements at 298 K showed that both linker functionalization and metal-node selection strongly affect uptake capacity. The novelty of this study lies in the side-by-side evaluation of two parent/amino-functionalized MOF pairs together with a Cu-based framework under the same adsorption conditions, allowing linker-functionalization effects to be distinguished from broader framework-dependent differences. Amino functionalization enhanced CO_2 uptake in the UiO-66 series from 1.98 to 2.74 mmol·g^{-1} at 1.0 bar, while the MOF-5 series remained below 0.4 mmol·g^{-1}. HKUST-1 exhibited the highest uptake of 4.39 mmol·g^{-1} at 1.0 bar, which may reflect contributions from accessible Cu^{2+} sites as well as differences in framework topology and porosity. These results highlight how linker functionalization and framework characteristics jointly influence CO_2 adsorption and provide a comparative basis for the design of MOF adsorbents.

Keywords: CO_2 capture; metal–organic frameworks; porous materials; gas adsorption

1. Introduction

Global climate change is intensifying, and CO_2 mitigation has become a major issue intimately tied to energy structure and sustainable development. Among the various mitigation technologies, adsorptive separation has attracted considerable attention because of its relatively low energy consumption and mild operating conditions [1,2]. However, existing adsorbents generally suffer from a difficult trade-off among capacity, stability, and regenerability: materials with high adsorption capacity often require high regeneration energy, materials with good stability frequently lack sufficient active sites, and materials with excellent low-pressure selectivity may be seriously affected by moisture or impurity gases. Therefore, simultaneously optimizing adsorption capacity, selectivity, and stability at the molecular level remains a central challenge in the design of CO_2 adsorbents [3].

To address this challenge, researchers have extensively explored materials such as porous carbons, zeolites, organic polymers, and MOFs [4–9]. Porous carbons possess high specific surface areas and good chemical stability, but their weak surface polarity limits their affinity for CO_2 [10]. Zeolites exhibit regular pores and good shape selectivity, yet their

Check for updates

Academic Editor: Cornelia Bandas

Received: 11 October 2026
Revised: 27 October 2026
Accepted: 29 October 2026
Published: 16 November 2026

Copyright: © 2026 by the authors. Licensee MDPI, Basel, Switzerland. This article is an open access article distributed under the terms and conditions of the Creative Commons Attribution (CC BY) license.

strongly polar pore walls make regeneration difficult [11,12]. Organic polymers offer flexible designability, but their high framework flexibility often compromises pore stability [13,14]. In contrast, MOFs, owing to the designability of their metal nodes and organic linkers, have become one of the fastest-growing classes of CO_2 adsorbents in recent years [3,15,16]. Previous studies have shown that amino functionalization can significantly enhance the low-pressure CO_2 uptake of MOFs, while open metal sites can provide strong directional interactions [3,17,18]. However, different frameworks respond inconsistently to the same functionalization strategy, and the synergistic mechanism between metal nodes and linkers remains unclear [19,20]. In particular, systematic comparisons of multiple MOFs under identical experimental conditions are still lacking.

In view of these deficiencies, this work adopts five representative MOFs as model systems and conducts an integrated study encompassing synthesis, characterization, adsorption evaluation, and comparative interpretation. First, MOF-5, MOF-5-NH_2, UiO-66, UiO-66-NH_2, and HKUST-1 are synthesized to establish a dual comparison of "same framework with different linkers" and "different metal nodes." Second, PXRD, UV–vis, SEM, and TGA are employed to confirm the structure, coordination environment, morphology, and thermal stability. Third, CO_2 adsorption–desorption isotherms are systematically measured at 298 K, with particular emphasis on the differences in adsorption capacity at 0.1 bar and 1.0 bar. Finally, by combining pore structure, polar functional groups, and open metal sites, a hierarchical "structure–interaction–adsorption" mechanism is proposed. The overall aim of this work is to answer the key scientific question of how metal nodes and organic linkers synergistically determine CO_2 adsorption performance [3,16].

2. Experimental Methods

2.1. Material Characterization Methods

All the chemicals are commercially available and used without further purification. Powder X-ray diffraction (PXRD) patterns were collected over approximately 3–50° in 2θ with a step size of 0.02° and a counting time of 0.5 s per step on a Bruker D8 Advance diffractometer (Bide Pharmatech Co., Ltd., Shanghai, China) using Cu Kα radiation. Scanning Electron Microscopy (SEM) images were acquired on a Sirion 200 (SEM) Field Emission Scanning Electron Microscope (Bide Pharmatech Co., Ltd., Shanghai, China) for qualitative assessment of particle morphology. Thermogravimetric Analysis (TGA) was carried out on a NETZSCH TG 209F1 Libra instrument (Bide Pharmatech Co., Ltd., Shanghai, China) from approximately 30 to 800 °C at 10 K·min^{-1} in open alumina crucibles, where the exported data list both air and nitrogen gas channels so that the active atmosphere and flow rate require confirmation from the original run settings, and the exported mass percentages were plotted without additional normalization; UV–vis traces were supplied over 200–500 nm using a Lambda 35 UV-vis Spectrometer (Perkin Elmer, Inc., Waltham, MA, USA).

2.2. The Preparation of MOFs

2.2.1. Synthesis of MOF-5 and MOF-5-NH_2

For MOF-5, terephthalic acid (H_2BDC; 0.420 g, 2.50 mmol) and zinc acetate dihydrate [$Zn(OAc)_2{\cdot}2H_2O$; 1.109 g, 5.00 mmol] were dissolved separately in dimethylformamide (DMF), using a total solvent volume of 40 mL. The two solutions were combined and stirred for 2.5 h. The precipitated solid was collected by centrifugation at 6000 rpm for 5 min and washed with DMF and methanol [21]. MOF-5-NH_2 was prepared under the same conditions using an equimolar amount of 2-aminoterephthalic acid (NH_2-H_2BDC; 0.453 g, 2.50 mmol) in place of H_2BDC.

2.2.2. Synthesis of UiO-66 and UiO-66-NH_2

UiO-66 was prepared using a half-scale adaptation of the reported solvothermal procedure. $ZrCl_4$ (1.46 g, 6.25 mmol), terephthalic acid (H_2BDC; 1.038 g, 6.25 mmol), and hydrochloric acid (37%; 0.537 mL, nominally 6.25 mmol) were combined in 30 mL of DMF. The mixture was sonicated for 30 min and transferred to a 60 mL Teflon-lined stainless-steel autoclave. The recorded thermal treatment was 493 K for 16 h. After cooling to room temperature, the solid was recovered by filtration, washed with methanol, and dried overnight at 423 K. UiO-66-NH_2 was prepared under the same recorded conditions using an equimolar amount of 2-aminoterephthalic acid (NH_2-H_2BDC; 1.132 g, 6.25 mmol) in place of H_2BDC.

2.2.3. Synthesis of HKUST-1

Benzene-1,3,5-tricarboxylic acid (H_3BTC; 1.05 g, 5.00 mmol) and copper(II) acetate monohydrate [$Cu(OAc)_2 \cdot H_2O$; 1.60 g, 8.00 mmol] were mixed in 200 mL of an H_2O/EtOH mixture (1:1, v/v) in a round-bottom flask. The reaction mixture was heated at 383 K for 4 h. The resulting solid was collected by centrifugation, washed four times with ethanol and water, and dried in air prior to characterization.

2.3. CO_2 Adsorption Performance Testing Method

CO_2 adsorption measurements. Pure-component CO_2 adsorption isotherms were measured on a Micromeritics ASAP 2020 Plus volumetric adsorption analyzer (Micromeritics, Norcross, GA, USA) to enable a quantitative comparison of gravimetric CO_2 uptake at 298 K and pressures up to approximately 1.0 bar; the sample masses entered in the instrument records were 0.1563 g for MOF-5, 0.1466 g for MOF-5-NH_2, 0.0914 g for UiO-66, 0.1143 g for UiO-66-NH_2, and 0.1187 g for HKUST-1. Because adsorption measurements were performed at a single temperature (298 K), temperature-dependent thermodynamic parameters such as the isosteric enthalpy of adsorption were not determined in the present study. Prior to each CO_2 adsorption measurement, all five MOF samples were degassed under vacuum at 100 °C for 15 h using the adsorption analyzer. The same degassing conditions were applied to all samples. The uptake values reported by the instrument were normalized to the sample mass entered for each measurement, which was used consistently as the gravimetric mass basis throughout the comparison. Measurements were conducted at 298 K using a circulating water bath and CO_2 with a reported purity of 99.999%; automatic thermal correction was enabled, and the warm and cold free-space volumes were measured for each sample. The programmed equilibration interval was 10 s, which represents the instrument setting used during equilibrium determination rather than a fixed total equilibration time for each pressure point, and since the exported reports do not provide a separate pressure-stability threshold, the reported points are described as instrument-accepted equilibrium measurements without claiming independent verification of complete equilibrium. Adsorbed volumes were exported in $cm^3 \cdot g^{-1}$ and converted to $mmol \cdot g^{-1}$ using a molar gas volume of 22.4 $L \cdot mol^{-1}$ [22].

3. Results and Discussion

3.1. Structural and Thermal Characterization of the MOFs

With the aim of elucidating the roles of metal nodes and organic linkers in governing CO_2 adsorption behavior, five MOFs, namely MOF-5, MOF-5-NH_2, UiO-66, UiO-66-NH_2, and HKUST-1, were synthesized according to the reported literature procedures. MOF-5 was prepared by reacting H_2BDC with $Zn(OAc)_2 \cdot 2H_2O$ in DMF at 298 K for 2.5 h, yielding a white powder with the characteristic PXRD reflections of MOF-5 (Figure 1a). Its framework consists of Zn_4O clusters interconnected by BDC^{2-} linkers in a three-dimensional

pcu topology (Figure 1g) [15,21]. Replacing H_2BDC with NH_2-H_2BDC under otherwise identical conditions afforded the isoreticular analogue MOF-5-NH_2 as an orange-red powder, in which NH_2-BDC^{2-} linkers bridge the Zn_4O clusters and the amino groups are oriented toward the pore interior (Figure 1a,j) [16,17]. UiO-66 and UiO-66-NH_2 were obtained by solvothermal treatment of $ZrCl_4$ with H_2BDC and NH_2-H_2BDC, respectively, in DMF containing hydrochloric acid, affording white and yellow powders that both showed the characteristic PXRD reflections of the UiO-66-type framework (Figure 1b) [17,23]. In these solids, twelve connected $Zr_6O_4(OH)_4$ clusters are linked by BDC^{2-} ligands into a three-dimensional fcu network, and replacing BDC^{2-} with NH_2-BDC^{2-} retains this topology while decorating the pore environment with amino groups (Figure 1h,k) [17,23]. In contrast, HKUST-1 was synthesized by a heated solution reaction between H_3BTC and $Cu(OAc)_2{\cdot}H_2O$, giving a blue powder with principal PXRD reflections consistent with crystalline HKUST-1, in which dinuclear $Cu_2(COO)_4$ paddlewheel units are interconnected by BTC^{3-} linkers into a tbo topology (Figure 1c,i,l) [24,25]. UV–vis spectroscopy provided complementary evidence for linker coordination. For example, UiO-66 exhibited a distinct absorption shoulder at approximately 270 nm, whereas free H_2BDC showed a resolved band near 239 nm, and comparable changes were observed for the other MOFs (Figure 1d–f). These spectral variations arise from changes in the electronic environments of the organic linkers upon coordination with the metal clusters. Together with the PXRD results, they support the successful formation of the five target MOFs.

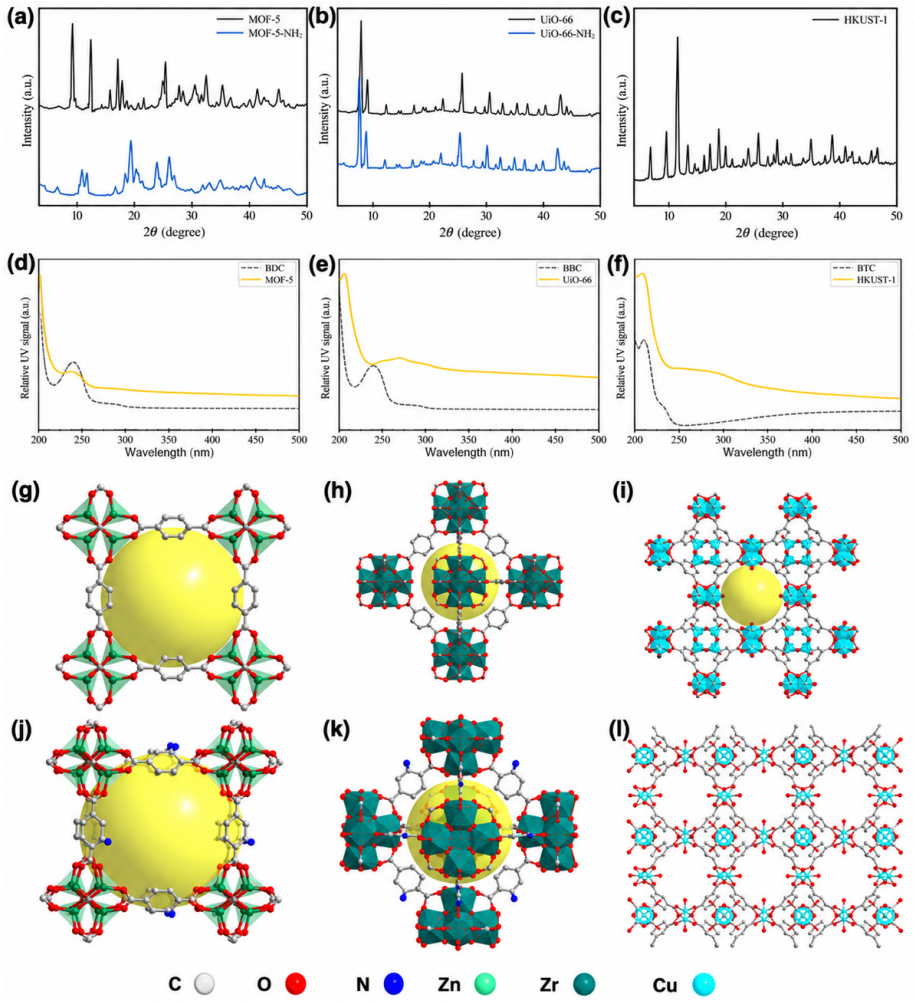


Figure 1. (**a**–**c**) Supplied PXRD patterns of the five MOFs. (**d**–**f**) UV–vis spectra of selected MOFs and the corresponding organic linkers. (**g**–**l**) Structural representations of the MOFs.

Furthermore, SEM analysis revealed distinct particle morphologies associated with the different metal–linker combinations (Figure 2). For instance, MOF-5 consisted mainly of agglomerated, faceted block-like crystallites, whereas MOF-5-NH_2 displayed a similar aggregated morphology but with smaller, less well-defined plate-like primary particles (Figure 2a,d) [26,27]. UiO-66 and UiO-66-NH_2 both formed compact, quasi-spherical aggregates of nanoscale primary particles, with UiO-66-NH_2 showing a more pronounced layered or petal-like surface texture (Figure 2b,e) [28]. HKUST-1 appeared as aggregates of irregular polyhedral particles, with no well-defined octahedral crystals observed (Figure 2c) [29]. Additionally, TGA was used to assess the thermal stability of the obtained materials. Low-temperature mass losses were attributed primarily to removal of physically adsorbed water and residual solvent, while the principal framework decomposition events occurred at approximately 567 °C for UiO-66-NH_2, 563 °C for UiO-66, 486 °C for MOF-5, 448 °C for MOF-5-NH_2, and 357 °C for HKUST-1 (Figure 2f). In this work, thermal stability was compared qualitatively using the temperature of the principal framework decomposition event observed in the TGA curves, with a higher decomposition temperature indicating greater resistance to thermal decomposition under the measurement conditions. On this basis, the overall thermal-stability order is UiO-66-NH_2 ≈ UiO-66 > MOF-5 > MOF-5-NH_2 > HKUST-1.

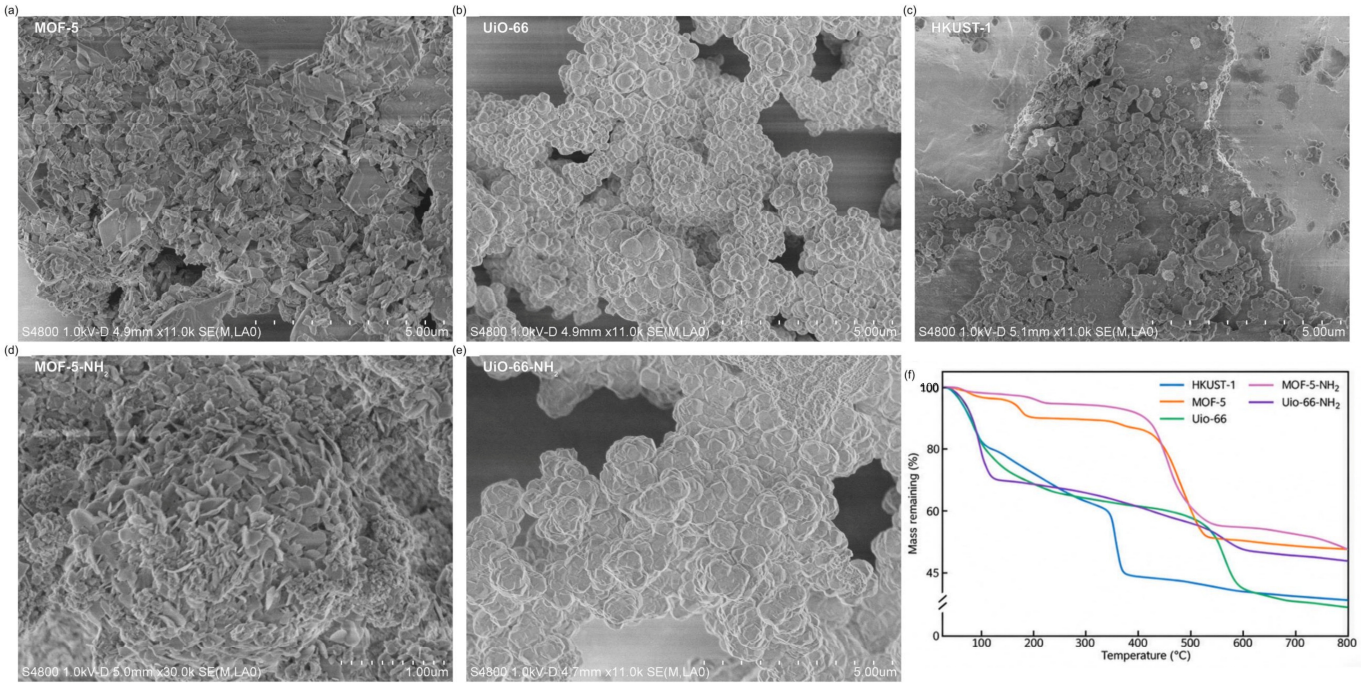


Figure 2. (**a**–**e**) SEM images of the five MOFs. (**f**) TGA curves of the MOFs.

3.2. CO_2 Adsorption Performance

The complete CO_2 adsorption and desorption isotherms of the five samples at 298 K are presented in Figure 3. The origin was included for all curves to provide a complete representation of their low-pressure adsorption behavior. For all samples, the CO_2 uptake increased continuously with pressure, and no fully developed saturation plateau was observed below approximately 1.0 bar. The desorption branches generally followed the corresponding adsorption branches, indicating that CO_2 adsorption was largely reversible under the measurement conditions, although the small differences between the two branches may reflect diffusion resistance or differences in pore accessibility.

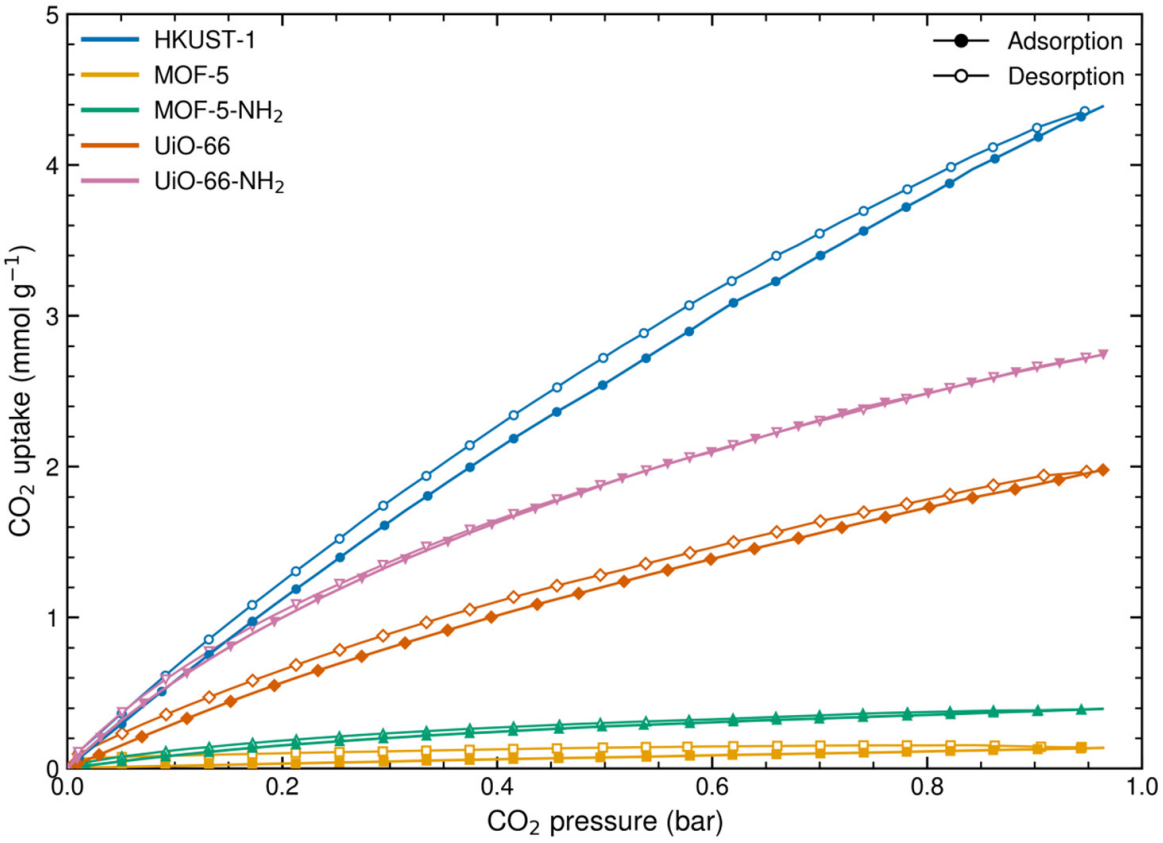


Figure 3. Complete CO_2 adsorption–desorption isotherms of HKUST-1, MOF-5, MOF-5-NH_2, UiO-66, and UiO-66-NH_2 measured at 298 K. Filled symbols represent the adsorption branches, and open symbols represent the desorption branches. Lines are included as guides to the eye.

At 1.0 bar, the CO_2 uptake capacities of the five MOFs exhibited pronounced structural dependence, with the performance ranking remaining consistent across the measured pressure range. A comparison of the two Zn-based materials clearly demonstrates the influence of linker functionalization. Both MOF-5 and its amino-functionalized counterpart, MOF-5-NH_2, displayed consistently low uptake across the entire measurement range (both <0.4 mmol·g^{-1}), with no discernible enhancement observed. In contrast, the UiO-66 series exhibited a well-defined linker modulation effect. At 0.1 bar, UiO-66 adsorbed 0.36 mmol g^{-1}, which increased to 0.59 mmol·g^{-1} upon amino functionalization (UiO-66-NH_2), corresponding to an absolute increase of 0.23 mmol·g^{-1} and a relative enhancement of 63.9% (Figure 3 and Table 1). At 1.0 bar, the uptake of UiO-66 reached 1.98 mmol·g^{-1}, while UiO-66-NH_2 further increased to 2.74 mmol·g^{-1}, representing an absolute increase of 0.76 mmol·g^{-1} and a relative enhancement of 38.4%. These results consistently indicate that linker amination effectively enhances the CO_2 uptake capacity of UiO-66. Among all five samples, HKUST-1 exhibited the highest CO_2 uptake, reaching 4.39 mmol·g^{-1} at 1.0 bar, which is approximately 1.6 times that of UiO-66-NH_2 and 2.2 times that of UiO-66, far exceeding the other materials. Overall, these results clearly reveal the significant impact of structural regulation strategies such as organic linker functionalization and metal node variation on the CO_2 adsorption performance of MOFs, providing a basis for the design of high-performance CO_2 adsorbents.

Table 1. Reported CO_2 uptake at 298 K and the calculated amino-functionalization effect for the UiO-66 pair.

Sample or Comparison	0.1 bar	1.0 bar
HKUST-1	Not reported	4.39
MOF-5	<0.4 *	<0.4 *
MOF-5-NH_2	<0.4 *	<0.4 *
UiO-66	0.36	1.98
UiO-66-NH_2	0.59	2.74
UiO-66 pair: absolute increase	0.23	0.76
UiO-66 pair: relative increase	63.9%	38.4%

Uptake and absolute differences are in $mmol \cdot g^{-1}$. The amino-functionalization effect was quantified in two ways. The absolute increase in CO_2 uptake was calculated as $\Delta q = q_{NH2} - q_{parent}$, while the relative increase was calculated as $[(q_{NH2} - q_{parent})/q_{parent}] \times 100\%$, where q_{NH2} and q_{parent} are the CO_2 uptake capacities of the amino-functionalized and parent MOFs, respectively, measured at the same temperature and pressure. * The upper bound is reported for the full measured range; exact endpoint values and uncertainties are not specified. "Not reported" does not mean zero. The MOF-5 and MOF-5-NH_2 assignments are supported by the overall PXRD correspondence. Values are rounded as in the reported dataset.

3.3. Mechanisms of CO_2 Adsorption

At the molecular level, the enhanced CO_2 uptake illustrated in the figure does not simply arise from differences in porosity or surface area, but rather from the synergistic interplay among pore confinement, local electrostatic environments, and specific adsorption sites, which collectively governs the adsorption energy and site occupancy of CO_2 within the framework [3,13]. In pristine MOF-5 and UiO-66, CO_2 molecules are primarily adsorbed through van der Waals interactions with the pore walls, confinement within microporous cavities, and electrostatic interactions between the quadrupole moment of CO_2 and the local electric fields of the framework, resulting in predominantly reversible physisorption (Figure 4) [3]. The incorporation of polar functional groups such as $–NH_2$ further strengthens CO_2 affinity by not only increasing the number of potential interaction sites but, more importantly, modulating the local electronic distribution and electrostatic potential within the pore channels. The N–H groups can establish weak hydrogen-bonding interactions with the oxygen atoms of CO_2, while the dipolar character and local electric fields associated with the amino groups enhance quadrupole–dipole interactions, thereby introducing a more specific component into the otherwise weak physisorption process [3,17]. Consequently, CO_2 adsorption in NH_2-functionalized MOFs is governed by the combined effects of pore confinement, electrostatic interactions, hydrogen bonding, and local charge redistribution, leading to enhanced CO_2 affinity relative to their parent frameworks [3,17]. Further enhancement can be achieved through metal-node engineering, as exemplified by activated HKUST-1. Removal of coordinated solvent molecules exposes open Cu^{2+} sites at the Cu_2 paddlewheel nodes, which possess pronounced Lewis acidity and can interact directionally with the lone-pair electrons of the oxygen atoms in CO_2. Meanwhile, the positively charged Cu^{2+} centers generate strong local electrostatic fields that effectively stabilize the quadrupole moment of CO_2. As a result, CO_2 preferentially occupies these energetically favorable open-metal sites at low surface coverage, giving rise to strong initial adsorption and enhanced low-pressure CO_2 affinity [3,24,25]. With increasing pressure, these high-energy sites become progressively occupied, and additional CO_2 molecules populate the cages, pore apertures, and other pore-wall regions, where van der Waals interactions, pore confinement, and adsorbate–adsorbate interactions become increasingly important [3]. Thus, the progressive increase in CO_2 uptake from MOF-5 ($0.14\ mmol \cdot g^{-1}$) and MOF-5–NH_2

(0.39 mmol·g^{-1}) to UiO-66 (1.98 mmol·g^{-1}), UiO-66–NH_2 (2.74 mmol·g^{-1}), and HKUST-1 (4.39 mmol·g^{-1}) can be understood as a consequence of the simultaneous enhancement of both the density and strength of accessible adsorption sites.

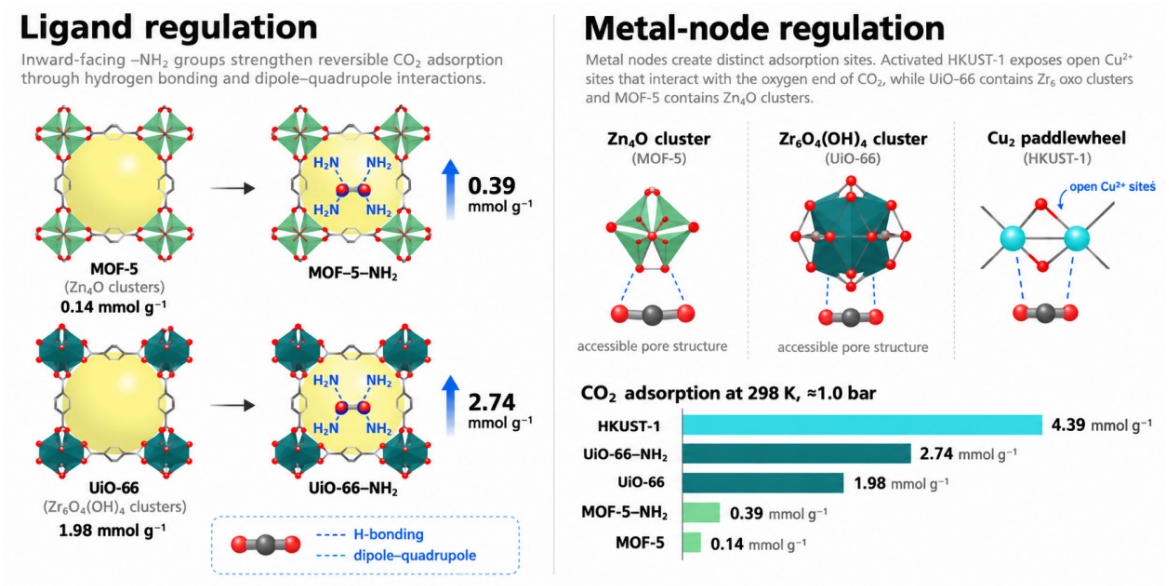


Figure 4. Schematic illustratlion of the proposed mechanisms of CO_2 interactions with the MOFs [3,17,19,24,25].

In this context, the pore structure primarily determines the accessibility and storage capacity for CO_2; ligand chemistry regulates the polarity and local electrostatic environment of the pore surface; and the metal nodes provide specific binding sites that determine the strength of host–guest interactions [3,24,25]. Overall, CO_2 adsorption in MOFs can therefore be viewed as a hierarchical structure–interaction–adsorption process, in which the balance between the available pore volume and the strength, density, and accessibility of specific adsorption sites ultimately dictates the macroscopic adsorption capacity and affinity [3,15,16].

4. Conclusions

The present study demonstrates that CO_2 adsorption in MOFs is governed by a hierarchical structure–interaction–adsorption mechanism. Pore structure determines accessibility and storage capacity, ligand chemistry regulates the polarity and local electrostatic environment of the pore surface, and metal nodes provide specific binding sites that dictate host–guest interaction strength. Within the UiO-66 family, amino functionalization increased CO_2 uptake from 1.98 to 2.74 mmol·g^{-1} at 1.0 bar, whereas the MOF-5/MOF-5-NH_2 pair remained below 0.4 mmol·g^{-1}. This contrast suggests that the effect of amino functionalization is framework-dependent. HKUST-1 showed the highest uptake of 4.39 mmol·g^{-1}, although this may reflect the combined effects of framework topology, porosity, and adsorption-site chemistry. Overall, these results indicate that effective MOF design should consider linker functionality together with framework structure and adsorption-site accessibility.

Author Contributions: Conceptualization, S.L. and X.K.; methodology, S.L. and X.K.; software, S.L. and Xing Kan; validation, Sharon Liang and Xing Kan; formal analysis, S.L.; investigation, S.L.; resources, S.L.; data curation, S.L.; writing—original draft preparation, S.L.; writing—review and editing, S.L. and Xing Kan; visualization, S.L.; supervision, X.K.; project administration, X.K.; funding acquisition, X.K. All authors have read and agreed to the published version of the manuscript.

Funding: This research received no external funding.

Data Availability Statement: The original contributions presented in this study are included in the article. Further inquiries can be directed to the corresponding author.

Conflicts of Interest: The authors declare no conflict of interest.

References

1. Boot-Handford, M.E.; Abanades, J.C.; Anthony, E.J.; Blunt, M.J.; Brandani, S.; Mac Dowell, N.; Fernández, J.R.; Ferrari, M.C.; Gross, R.; Hallett, J.P.; et al. Carbon Capture and Storage Update. *Energy Environ. Sci.* **2014**, *7*, 130–189. [CrossRef]
2. Rochelle, G.T. Amine Scrubbing for CO_2 Capture. *Science* **2009**, *325*, 1652–1654. [CrossRef] [PubMed]
3. Sumida, K.; Rogow, D.L.; Mason, J.A.; McDonald, T.M.; Bloch, E.D.; Herm, Z.R.; Bae, T.-H.; Long, J.R. Carbon Dioxide Capture in Metal-Organic Frameworks. *Chem. Rev.* **2012**, *112*, 724–781. [CrossRef] [PubMed]
4. Xia, T.; Wu, Y.; Ji, T.; Hu, W.; Yu, K.; He, X.; Yin, B.H.; Liu, Y. Mixed-matrix membranes incorporating hierarchical ZIF-8 towards enhanced CO2/N2 separation. *Smart Mol.* **2025**, *3*, e20240066. [CrossRef] [PubMed]
5. Molavi, H.; Mirzaei, K.; Barjasteh, M.; Rahnamaee, S.Y.; Saeedi, S.; Hassanpouryouzband, A.; Rezakazemi, M. 3D-Printed MOF Monoliths: Fabrication Strategies and Environmental Applications. *Nano-Micro Lett.* **2024**, *16*, 272. [CrossRef] [PubMed]
6. Zhou, H.; Ren, Z.; Xu, C.; Xu, L.; Lee, C. MOF/Polymer-Integrated Multi-Hotspot Mid-Infrared Nanoantennas for Sensitive Detection of CO2 Gas. *Nano-Micro Lett.* **2022**, *14*, 207. [CrossRef] [PubMed]
7. Li, D.; Ye, M.; Ma, C.; Li, N.; Gu, Z.; Qiao, Z. Preparation of a self-supported zeolite glass composite membrane for CO2/CH4 separation. *Smart Mol.* **2024**, *2*, e20240009. [CrossRef] [PubMed]
8. Guo, Y.; Cui, X.; Cui, Y.; Li, Z.; Tosheva, L.; Li, X.; Guo, H. Phenolic Resin-Functionalized NH2-UiO-66-Containing Mixed Matrix Membranes for CO2/CH4 Separation. *EcoEnergy* **2026**, *00*, e70116. [CrossRef]
9. Chen, J.; Wang, Y.; Yu, Y.; Wang, J.; Liu, J.; Ihara, H.; Qiu, H. Composite materials based on covalent organic frameworks for multiple advanced applications. *Exploration* **2023**, *3*, 20220144. [CrossRef] [PubMed]
10. Sevilla, M.; Mokaya, R. Energy Storage Applications of Activated Carbons: Supercapacitors and Hydrogen Storage. *Energy Environ. Sci.* **2014**, *7*, 1250–1280. [CrossRef]
11. Joos, L.; Swisher, J.A.; Smit, B. Molecular Simulation Study of the Competitive Adsorption of H_2O and CO_2 in Zeolite 13X. *Langmuir* **2013**, *29*, 15936–15942. [CrossRef] [PubMed]
12. Wang, Y.; LeVan, M.D. Adsorption Equilibrium of Binary Mixtures of Carbon Dioxide and Water Vapor on Zeolites 5A and 13X. *J. Chem. Eng. Data* **2010**, *55*, 3189–3195. [CrossRef]
13. Ozdemir, J.; Mosleh, I.; Abolhassani, M.; Greenlee, L.F.; Beitle, R.R., Jr.; Beyzavi, M.H. Covalent Organic Frameworks for the Capture, Fixation, or Reduction of CO_2. *Front. Energy Res.* **2019**, *7*, 77. [CrossRef]
14. Zeng, Y.; Zou, R.; Zhao, Y. Covalent Organic Frameworks for CO_2 Capture. *Adv. Mater.* **2016**, *28*, 2855–2873. [CrossRef] [PubMed]
15. Furukawa, H.; Cordova, K.E.; O'keeffe, M.; Yaghi, O.M. The Chemistry and Applications of Metal-Organic Frameworks. *Science* **2013**, *341*, 1230444. [CrossRef] [PubMed]
16. Yaghi, O.M.; Li, Q. Reticular Chemistry and Metal-Organic Frameworks for Clean Energy. *MRS Bull.* **2009**, *34*, 682–690. [CrossRef]
17. Luan, Y.; Qi, Y.; Gao, H.; Andriamitantsoa, R.S.; Zheng, N.; Wang, G. A general post-synthetic modification approach of amino-tagged metal-organic frameworks to access efficient catalysts for the Knoevenagel condensation reaction. *J. Mater. Chem. A* **2015**, *3*, 17320–17331. [CrossRef]
18. Yang, Z.; Li, X.; Cui, X.; Zheng, Z.; Zheng, P.; Zhang, Y. Integrated Strategies Toward the Capture and Electrochemical Conversion of Low-Concentration Carbon Dioxide. *Exploration* **2025**, *5*, e20240006. [CrossRef] [PubMed]
19. Burtch, N.C.; Jasuja, H.; Walton, K.S. Water Stability and Adsorption in Metal-Organic Frameworks. *Chem. Rev.* **2014**, *114*, 10575–10612. [CrossRef] [PubMed]
20. Thornton, A.W.; Babarao, R.; Jain, A.; Trousselet, F.; Coudert, F.-X. Defects in metal-organic frameworks: A compromise between adsorption and stability? *Dalton Trans.* **2016**, *45*, 4352–4359. [CrossRef] [PubMed]
21. Peng, M.; Jeon, U.; Ganesh, M.; Aziz, A.; Vinodh, R.; Palanichamy, M.; Jang, H.T. Oxidation of Ethylbenzene Using Nickel Oxide Supported Metal Organic Framework Catalyst. *Bull. Korean Chem. Soc.* **2014**, *35*, 3213–3218. [CrossRef]
22. Thommes, M.; Kaneko, K.; Neimark, A.V.; Olivier, J.P.; Rodriguez-Reinoso, F.; Rouquerol, J.; Sing, K.S.W. Physisorption of gases, with special reference to the evaluation of surface area and pore size distribution (IUPAC Technical Report). *Pure Appl. Chem.* **2015**, *87*, 1051–1069. [CrossRef]
23. Bueken, B.; Van Velthoven, N.; Willhammar, T.; Stassin, T.; Stassen, I.; Keen, D.A.; Baron, G.V.; Denayer, J.F.M.; Ameloot, R.; Bals, S.; et al. Gel-Based Morphological Design of Zirconium Metal-organic Frameworks. Author manuscript. *arXiv* **2016**, arXiv:1612.00699. [CrossRef]
24. Yang, A.; Li, P.; Zhong, J. Facile preparation of low-cost HKUST-1 with lattice vacancies and high-efficiency adsorption for uranium. *RSC Adv.* **2019**, *9*, 10320–10325. [CrossRef] [PubMed]

25. Jiang, L.L.; Zeng, X.; Li, M.; Wang, M.-Q.; Su, T.-Y.; Tian, X.-C.; Tang, J. Rapid electrochemical synthesis of HKUST-1 on indium tin oxide. *RSC Adv.* **2017**, *7*, 9316–9320. [CrossRef]
26. Jasim, S.; Amin, H.M.; Rajabizadeh, A.; Nobre, M.A.L.; Borhani, F.; Jalil, A.T.; Saleh, M.M.; Kadhim, M.M.; Khatami, M. Synthesis characterization of Zn-based MOF and their application in degradation of water contaminants. *Water Sci. Technol.* **2022**, *86*, 2303–2335. [CrossRef] [PubMed]
27. Abeysinghe, A.K.; Peng, Y.P.; Huang, P.J.; Chen, K.F.; Chen, C.H.; Chen, W.X.; Liang, F.Y.; Chien, P.Y. Enhancing visible-light-driven photocatalysis: Unveiling the remarkable potential of H_2O_2-assisted MOF/COF hybrid material for organic pollutant degradation. *Environ. Sci. Pollut. Res.* **2024**, *31*, 50983–50999. [CrossRef] [PubMed]
28. Xue, Y.; Chew, J.W. UiO-66 (Zr) metal–organic framework for photocatalytic CO_2 reduction: Functional design strategies for sustainable carbon utilization. *J. Mater. Chem. A* **2025**, *13*, 11989–12008. [CrossRef]
29. Ediati, R.; Laharto, P.; Safitri, R.; Mahfudhah, H.; Sulistiono, D.O.; Syukrie, T.D.; Nadjib, M. Synthesis of HKUST-1 with addition of Al-MCM-41 as adsorbent for removal of methylene blue from aqueous solution. *Mater. Today Proc.* **2020**, *46*, 1799–1806. [CrossRef]

Disclaimer/Publisher's Note: The statements, opinions and data contained in all publications are solely those of the individual author(s) and contributor(s) and not of MDPI and/or the editor(s). MDPI and/or the editor(s) disclaim responsibility for any injury to people or property resulting from any ideas, methods, instructions or products referred to in the content.